Batteries & Supercaps

Research Article
doi.org/10.1002/batt.202400063

Chemistry Europe
European Chemical Societies Publishing

www.batteries-supercaps.org

Advanced Electrode Materials Based on Brownmillerite Calcium Ferrite for Li-Ion Batteries

Guido Spanu,[a, b] Arcangelo Celeste,[a, b] Francesco Bozza,[a] Emanuele Serra,[c] Piero Torelli,[d] Luca Braglia,[d, e] Sergio Brutti,[b] Priscilla Reale,[f] and Laura Silvestri*[a]

Iron-based materials are considered potential anode materials for lithium-ion batteries thanks to their low cost, abundancy, non-flammability, good safety, environmental benignity, and high specific capacity. Here, a series of calcium iron oxides materials having brownmillerite structure (i.e., $Ca_2Fe_{2-x}M_xO_5$, where M=Mn, Ni and Cu and x = 0 and 0.1) has been extensively studied for their use as conversion anodes in lithium cell. In particular, a mechanochemical approach has been used either to synthesize the samples and to prepare electrodes for the tests in lithium cell. $Ca_2Fe_2O_5$ based electrodes proved excellent performance in lithium cell, approaching the theoretical capacity and being stable upon prolonged cycling (529 mAh g^{-1} at C/10 and a capacity retention of 81% after 100 cycles). Through the use of ex-situ diffraction measurements, we have analyzed the conversion mechanism and proved the partial reversibility of its electrochemical reaction. Also, the incorporation of dopants into the structure of calcium iron oxide resulted in further improvement of its electrochemical performance as is the case of Mn doped sample that show a considerable specific capacity of 567 mAh g^{-1} and the capacity retention is almost 99% after 100 cycles.

Introduction

The booming of battery demand worldwide is making even more urgent compared to the recent past the need of innovations in materials for lithium-ion batteries.[1,2] Lithium-ion batteries need to increase their storage capacity and intrinsic safety at lower price, in a highly competitive market. These challenges are extremely hard to solve exploiting the established materials chemistries (i.e. carbons, Co-based layered oxides, silicon) also in consideration of the vulnerabilities in their supply chain.[3,4] In fact, the inhomogeneous distribution across the globe of raw materials mines as well as the electrode production factories puts at risk the future expansion and stability of the battery market worldwide.[1–6] Therefore, new materials are need with (a) large practical capacity values, (b) minimal content of critical raw materials, and (c) manufacture through an easily scalable synthesis.

On the negative electrode side, iron oxides-based conversion materials are a possible solution to tackle these challenges. This class of materials is consisted by binary iron oxides, such as Fe_2O_3 or Fe_3O_4, but also different types of ternary materials, such as MFe_2O_4 (being M a divalent metal stable in its 2+ oxidation state like Zn, Ni, Mn, Cu among others) or $Ca_2Fe_2O_5$.[7,8] In batteries, these compounds can react with lithium ions through conversion reactions.[7–9] During the reduction step, conversion processes lead to the formation of Li_2O and metal particles. In the case of ternary iron oxides, the third atomic constituent of the pristine materials (M in the above formula) can participate or promote alloying reactions, as is the case of Zn, or can support a reversible reaction evolution by providing a suitable and invariant morphological matrix, as is the case of Ca.[8,10]

Iron-based oxides can be synthetized starting from a very common commodity on the crust earth, such as hematite, and they have a higher theoretical capacity compared to graphite (372 mAh g^{-1}) ranging between 1007 (i.e. Fe_2O_3) to 438.3 mAh g^{-1} (i.e. $Sr_2Fe_2O_5$) depending on the stoichiometry and on the identity of the divalent metal.[8] However, the low stability of conversion anodes over cycling hinders their further development for commercial purposes.[8]

Among the different ternary iron oxides, the brownmillerite-type calcium ferrite, $Ca_2Fe_2O_5$, (CFO) has been scarcely inves-

[a] G. Spanu, A. Celeste, F. Bozza, L. Silvestri
Dipartimento di Tecnologie Energetiche e Fonti Rinnovabili ENEA,
Agenzia Nazionale per le Nuove Tecnologie,
l'Energia e lo Sviluppo Economico Sostenibile C.R.
Casaccia, via Anguillarese 301, 00123, Roma (Italy)
E-mail: laura.silvestri@enea.it

[b] G. Spanu, A. Celeste, S. Brutti
Dipartimento di Chimica
Sapienza Università di Roma p.le Aldo Moro 5, 00185, Roma (Italy)

[c] E. Serra
Dipartimento di Sostenibilità dei Sistemi Produttivi e Territoriali ENEA,
Agenzia Nazionale per le Nuove Tecnologie,
l'Energia e lo Sviluppo Economico Sostenibile C.R.
Casaccia, via Anguillarese 301, 00123, Roma (Italy)

[d] P. Torelli, L. Braglia
Istituto Officina Materiali
CNR, Consiglio Nazionale della Ricerca
IOM-CNR ss 14, km 163.5, 34149 Basovizza (Italy)

[e] L. Braglia
Istituto Ricerca e Innovazione Tecnologica (RIT)
Area Science Park
Padriciano 99, 34149 Trieste (Italy)

[f] P. Reale
Dipartimento di Fusione e tecnologie per la Sicurezza Nucleare ENEA,
Agenzia Nazionale per le Nuove Tecnologie,
l'Energia e lo Sviluppo Economico Sostenibile C.R.
Frascati, via E.Fermi 45, 00044 Frascati (Italy)

Supporting information for this article is available on the WWW under https://doi.org/10.1002/batt.202400063

Research Article
doi.org/10.1002/batt.202400063
Chemistry Europe
European Chemical Societies Publishing

tigated as a conversion anode despite its promising reversibility upon cycling.[9–13] Brownmillerite structure consists in a perovskite-like lattice with ordered and periodic oxygen vacancy motifs. The presence of (1/6) oxygen vacancies along [101] direction starting from the original perovskite unit cell leads to a major alteration in the first neighbor shell of part of iron cations, shifting from a local octahedral coordination to a tetrahedral one. Therefore, the structure can be seen as a stacking sequence of layers constituted by alternated FeO_6 and FeO_4 units along the b-axis. This peculiar structure is effective in many different electrochemical applications such as solid fuel cells,[14] CO_2 capture,[15] photodegradation of organic fluent,[16] catalyst for oxidation processes.[17] Because of all these applications, different synthetic routes have been reported so far in the literature for the synthesis of polycrystalline[18–22] and monocrystalline[23,24] CFO comprising sol-gel syntheses,[18,20] solid-state reaction[9,25] or solid-state reaction with High-Energy-Ball-Milling (HEBM) as activation step.[21,26,27]

Here, we demonstrate the CFO conversion anode for lithium-ion batteries, synthesized using a novel synthesis route and we investigate the effect of doping on the crystal structure and the corresponding electrochemical properties.

CFO nanoparticles have been synthesized by a solid-state synthetic route with dry HEBM. This method does not require any kind of organic solvent and is easily scalable. Furthermore, most of reactants are extremely abundant materials such as Fe_2O_3 and $CaCO_3$. This synthetic route allows the facile preparation of undoped and doped brownmillerite, with different types of dopants (i.e., Mn, Ni or Cu). Overall, doping the calcium ferrite leads to structural and morphological changes as shown here using various experimental techniques.

Overall doped iron ferrite shows improved performance as conversion anode for lithium-ion cells, in terms of capacity retention and cycling stability compared to the state-of-the-art. The conversion reaction has been also characterized by means of ex situ X-Ray Diffraction (XRD) thus disclosing additional insights about the phase transformations during galvanostatic charge and discharge in a lithium cell. Therefore, we demonstrated as calcium ferrites can be promising alternatives to graphitic anodes, as cheap and green materials for Li-ion batteries.

Table 1. List of the samples under investigation and label used.

Sample name	M	Formula
CFO	/	$Ca_2Fe_2O_5$
CFMO	Mn	$Ca_2Fe_{1.9}Mn_{0.1}O_5$
CFNO	Ni	$Ca_2Fe_{1.9}Ni_{0.1}O_5$
CFCO	Cu	$Ca_2Fe_{1.9}Cu_{0.1}O_5$

Results and Discussion

Synthesis Assessment

Four (4) samples have been synthesized and investigated: all materials have the general formula $Ca_2Fe_{2-x}M_xO_5$ where M = Mn, Ni or Cu and x = 0 and 0.1. Materials coding and compositions are reported in the Table 1 and all cations stoichiometric ratios have been confirmed by atomic absorbance (Table S1).

CFO phase identity has been evaluated from XRD and Raman spectroscopy. XRD experimental pattern, shown in Figure 1a, matches with the reported pattern of $Ca_2Fe_2O_5$ (PDF file number 00-047-1744) crystallizing in orthorhombic system

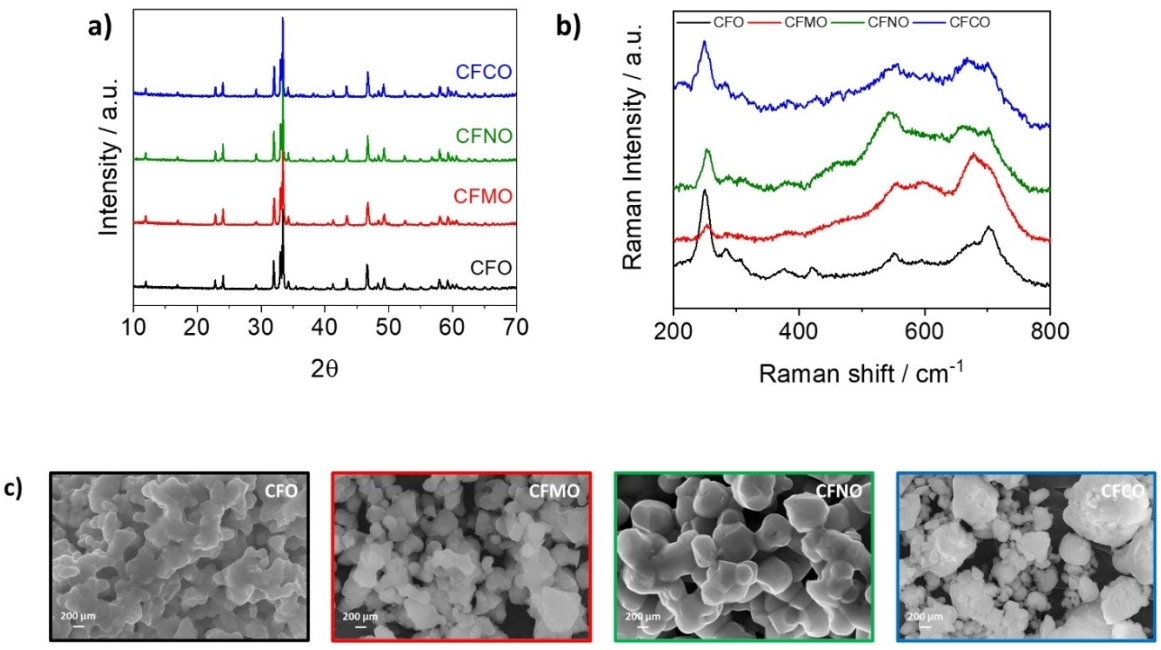

Figure 1. Experimental a) XRD pattern, b) Raman spectra and c) SEM micrographs of the undoped $Ca_2Fe_2O_5$ (CFO) and doped samples.

with spatial groups *Pnma*.[28] Diffraction peaks are sharp and intense, indicating the high crystallinity of the powders. Phase purity and lattice parameters have been determined using GSAS-II.[29] The experimental and fitted XRD patterns are shown in Figure S1. Calculated cell parameters are equal to a = 5.424 Å, b = 14.792 Å, and c = 5.595 Å, with 0.1803 μm size and micro strain of 3314.3.

Turning to the doped CFOs, XRD (see the Figure 1a) confirm the formation of the brownmillerite prototypal structure in all cases, being the patterns easily indexed to the expected orthorhombic lattice with the spatial group *Pnma*. Also in these cases Rietveld Refinements have been carried out in order to evaluate the effect of doping on crystal structure and estimate cell parameters for all doped samples (see Figure S2 and Table 2). The refined crystal structures highlight the evident deformation of the unit cell with the doping. This distortion is qualitatively very similar while comparing the different dopants: overall *a* and *c* parameters decrease whereas the *b* axis increases in size. The extent of the lattice distortion is however different among the dopant, being the *b* parameter of the CFCO sample the most expanded among all. Overall, lattice parameters variation leads to a slight volume contraction in the doped samples compared to the undoped one, being more evident in the CFMO and CFNO cases. The packing factor (PF), $PF = \Sigma iVi/Vcell$, has been calculated using the refined crystallographic data and the Shannon radii. A value of 0.59 was obtained for all materials due to the small amount of dopants and the very similar Shannon radius. Such results agree with the results in literature and are indirect evidence of the incorporation of dopants within the orthorhombic lattice.[28]

Raman spectroscopy confirmed the formation of the brownmillerite phase. In fact, this crystal structure shows 105 normal modes of which 48 are Raman Active.[30] However, only few of these can be observed in the 200–800 cm^{-1} region. From literature,[19,30–33] only 9 bands are a specific fingerprint of the formation of the brownmillerite phase, namely at 254, 290 312, 379, 395, 427, 555, 667, 706 and 740 cm^{-1}. All the bands, except those at 667 and 740 cm^{-1}, can be assigned to modes with A_g symmetry, whilst the others show B_g symmetry.[30,32]

The experimental Raman spectrum of the CFO undoped sample shown in Figure 1b, nicely matches the expected vibrational fingerprint of the brownmillerite lattice. Similar spectra and vibrational assignments are observed for the doped materials with few differences in intensities and shifts, as shown in Figure 1b. These alterations of the vibrational spectra are another independent clue of the doping of the pristine orthorhombic lattice. In one with the structural observations derived by XRD, also in the case of Raman spectra, the entity of the distortions in the vibrational bands varies among the samples depending on the dopant specie. Apparently, while some bands are unchanged, such as A_g mode at 380 cm^{-1} for CFNO, others are much more affected by the incorporation of dopants in the lattice. As an example, the A_g mode at 255 cm^{-1} (CFO) shows a peak intensity decrease and blue or red shift in the doped samples. This mode shifts to 253, 260 and 253 cm^{-1} for CFNO, CFCO and CFMO, respectively. Unfortunately, without a detailed modeling of the phonon spectra, additional speculations would be too tentative. However, this is beyond the scope of the manuscript also in consideration of the dependance of Raman bands from additional physico-chemical factors such as crystal orientation, particle size, disorder and, in few cases, from the excitation energy.[30,32]

The morphology of all the samples has been analyzed by FEG-SEM at different magnifications. SEM micrographs of CFO sample in Figure 1c show a material formed by prismatic particles of similar diameters, i.e., ~200 nm. Dopants alter the morphology of original material to a different extent. The incorporation of manganese in the lattice does not determine any type of morphological changes, whilst nickel promotes a neat increase of particle size, 500 nm, and shapes modification, more cubic particles. Turning to CFCO, morphology is drastically changed and particles with diameters bigger than 100 μm formed by the strong agglomeration of smaller particles are observed. EDX maps shown in Figure S3 confirms a homogenous distribution of dopants across the particles for all samples, thus confirming the lack of phase segregation.

The surface chemistry of the different samples was studied with X ray photoemission spectroscopy. The core levels of the samples were all identified (Figure S4). No impurities were detected, except for additional peaks of Cu and Mo coming from the sample holder and the presence of some Carbon due to air exposure during sample mounting. The concentration of doping metals (Cu, Mn, and Ni) is too small to be detected using the XPS technique which means that in the surface layer their relative concentration is roughly below 1%. The Calcium peaks are well visible, and this permits the analysis of the Ca chemical state in depth. The oxidation state of Ca is consistently 2+ for all the samples, as illustrated in Figure 2a. Additionally, there is a slight broadening of the 2pCa peaks for the CFNO and CFO samples, noticeable in the shallower valley at 351 eV that can be attributed to the presence of more disordered Ca sites.

Furthermore, the core level shape of 2p Fe is remarkably similar for all the samples (Figure 2b). The energy position of

Table 2. Lattice phase cell parameters (a, b, c) with its volume (V) and weighted-profile residuals (R_{wp}) and chi-squared (χ^2) calculated for the doped samples by Rietveld Refinement.

Sample name	a (Å)	b (Å)	c (Å)	V (Å^3)	R_{wp} (%)	χ^2
CFO	5.424	14.791	5.595	448.9	20.99	2.2
CFMO	5.419	14.802	5.584	447.9	20.76	2.1
CFNO	5.413	14.804	5.590	447.9	20.54	2.4
CFCO	5.416	14.833	5.586	448.7	19.55	1.7

Research Article
doi.org/10.1002/batt.202400063
Chemistry Europe
European Chemical Societies Publishing

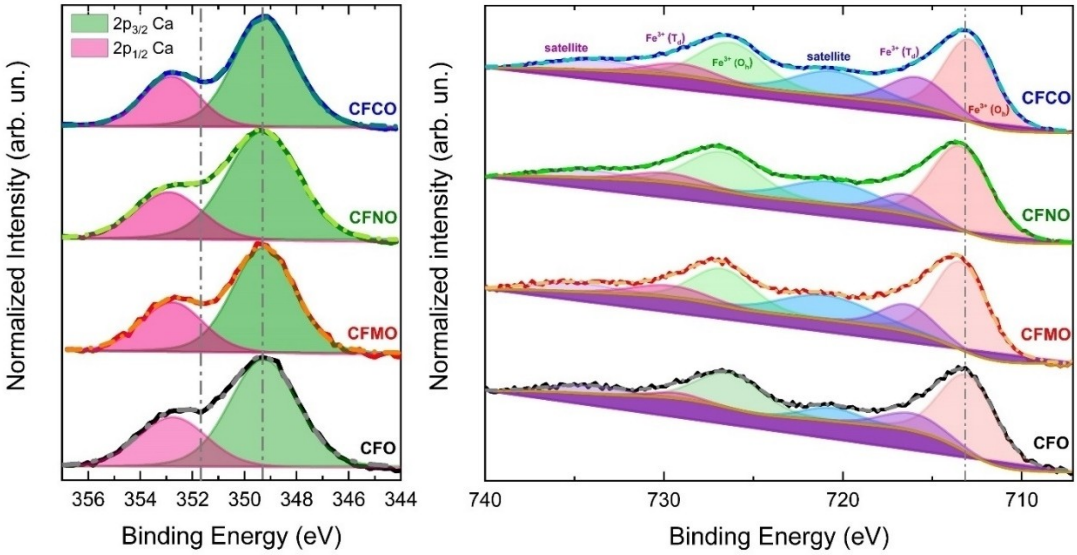

Figure 2. a) Normalized 2p Ca core level and b) Normalized 2pFe core level of CFO (black), CFMO (red), CFCO (blue), CFNO (green). The fits are reported in dashed line while the shadow indicates the single component considered in the fit.

the Fe 2p core level for all samples indicates a Fe^{3+} site as the main component.[34] However, the fit analysis in Figure 2b reveals two distinct Fe^{3+} species: one at approximately 713 eV ($2p_{3/2}$) −726.3 eV ($2p_{1/2}$) and the other, less intense, at around 716 eV ($2p_{3/2}$) 734.3 eV ($2p_{1/2}$). The former can be attributed to Fe^{3+} in octahedral (O_h) geometry within FeO_6 units, while the latter corresponds to Fe^{3+} in tetrahedral (T_d) geometry within FeO_4 units.[35,36] The content of the Fe^{3+} T_d phase was assessed by calculating the ratio between the area of the Fe^{3+} T_d peak and the sum area of $T_d + O_h$. The %Td trend is CFCO (28.9%) > CFMO (23.6%) > CFO (19.7%) > CFNO (16.2%).

In order to further investigate the doping effect, electrical conductivity measurements have been carried out. The electrical conductivity (see Table S2) of the undoped material was in the order of 10^{-7} S·cm^{-1}. While Mn doping does not affect conductivity and Ni doping produces only a small increase ($9.8 \cdot 10^{-6}$ S·cm^{-1}), Cu doping causes an impressive improvement of several order of magnitude, to $2.5 \cdot 10^{-2}$ S·cm^{-1}.

CFO Electrodes: Electrochemical Behavior in Lithium Cell

To evaluate the electrochemical activity of CFOs samples in lithium cell, electrodes have been manufactured by mixing CFO powder and SuperP carbon through HEBM for 5 hours. The addition of SuperP by HEBM leads to the formation of a CFO/carbon composite that has two main advantages compared to the pristine oxide powder: (i) the presence of the SuperP improve the electrical conductivity and (ii) the homogeneous distribution of carbon enveloping the CFO particles alleviate the volumetric changes occurring during the conversion reaction. The XRD pattern shown in Figure S5 confirms that CFO keeps the same phase after ball milling with carbon. Furthermore, SEM observations shown in Figure S5 confirm the formation of a composite material where ferrites particles are homogeneously surrounded by SuperP particles.

Electrochemical performance in lithium cell has been investigated by galvanostatic cycling with a current density of 59 mA g^{-1} (C/10) between 0.005-3 V vs Li/Li$^+$ as shown in the Figure 3a where charge/discharge potential profiles obtained for CFO electrodes at different cycles are illustrated.

The potential profile of CFO in first discharge (reduction) shows a rapid drop till 1.5 V vs Li. At smaller potential a little slope can be assigned to the formation of a passivating layer on carbon.[9] At potentials below 1 V vs Li, a long plateau at ~0.5 V vs Li occurs (Q = 600 mAh g^{-1}). The plateau is preceded and followed by two sloping regions. According to literature, these regions can be associated to the conversion reaction of calcium ferrites and related processes.[9,10]

Overall, the conversion reaction involves the reduction of the calcium ferrite phase and the consequent formation of three different solid phases: iron metal, Fe, calcium oxide, CaO, and lithium oxide, Li_2O, in the discharge stage (reduction). The general process is: $Ca_2Fe_2O_5 + 6Li^+ + 6e^- \rightarrow 2CaO + 2Fe + 3Li_2O$. The process has a theoretical specific capacity of ca. 591 mAh g^{-1}. However, at the end of first discharge specific capacity of ca. 1200 mAh g^{-1} have been exchanged. Furthermore, upon re-charge, only a small part of this capacity is returned in the sloping process above 1 V, as evident from the unsatisfactory Coulombic efficiency value (48%) in the first cycle. The discrepancy between theoretical and experimental first discharge specific capacity and the low Coulombic efficiency can be related to inherent irreversible contributions of conversion reaction and SEI formation.[7–10,37,38] From the second cycle, the potential profile changes and only the process below 1 V vs Li remains stable upon cycling. In fact, as shown in Figure 3a, a specific capacity of ca. 600 mAh g^{-1} is exchanged reversibly. Furthermore, from the cycling performance in Figure 3b, an initial increase of specific capacity during the first ten cycles

Research Article
doi.org/10.1002/batt.202400063
Chemistry Europe
European Chemical Societies Publishing

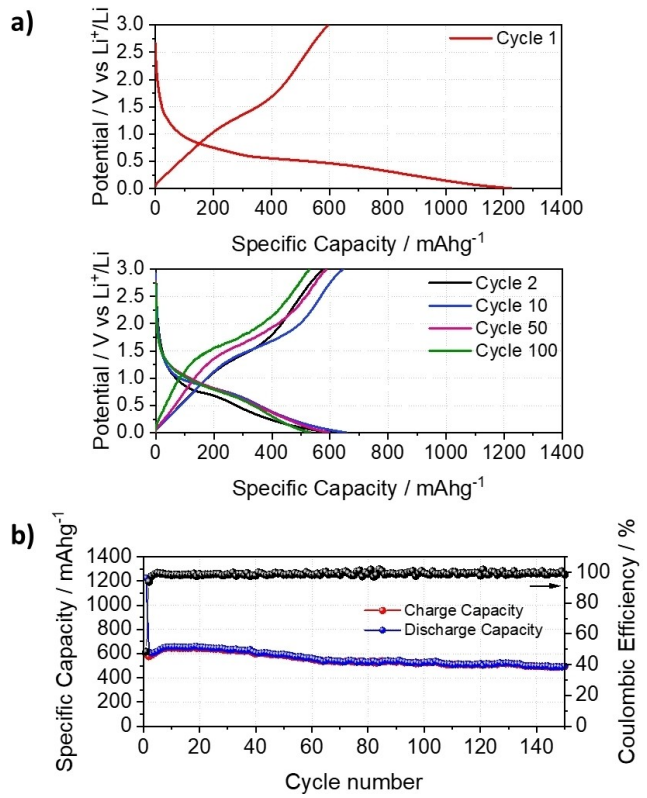

Figure 3. a) Potential profiles, b) Specific Capacity and Coulombic efficiency as function of cycle numbers obtained for CFO-based electrodes in galvanostatic mode at C/10.

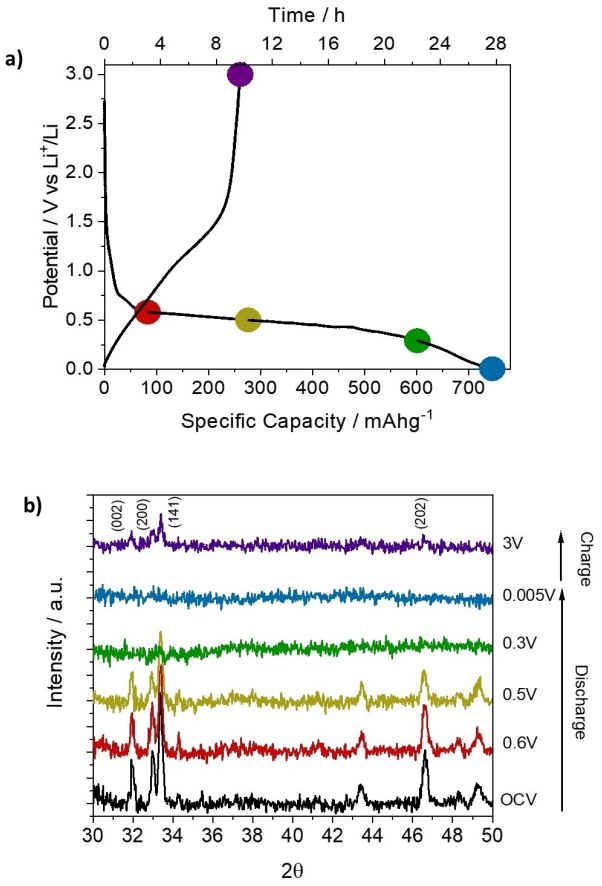

Figure 4. a) Potential profile of CFO electrodes in lithium cell indicating the points where the measure has been interrupted and the corresponding b) XRD patterns acquired at the different state of discharge/recharge.

occurs, and it can be related to the uncomplete reaction of CFO during first discharge. After 100 cycles, capacity is still around 529 mAh g^{-1}, corresponding to a capacity retention of 81 %.[9–11] Unfortunately, the performance evaluation cannot provide an exhaustive description of the structural transformations underlying the electrochemical traces. Therefore, an additional technique is needed for a full characterization of chemical processes occurring along the plateau. In the literature conversion reaction is associated to the disruption of a crystalline phase, $Ca_2Fe_2O_5$, and the formation of new ones, Fe, Li_2O, CaO.

Thus, XRD can be a suitable technique to study more in-depth structural transformations associated to conversion reactions.[37,39]

Specific self-standing electrodes have been submitted to controlled electrochemical processes and then investigated by XRD. Self-standing samples have been used, instead of the standard electrode coated onto the copper foil, to remove support interference in the diffractograms. In order to highlight the electrochemical incorporation mechanism, XRD measurements have been taken by interrupting galvanostatic discharging/charging at specific points of voltage curves, as shown in Figure 4a. When discharged to 0.6 V (after 4 h) some peaks of CFO, such as (002) and (141), show an evident decrease, whilst others, like (200), remain almost unchanged. Furthermore, slight shifts can be observed for all the cited three peaks. This picture is coherent to a partial incorporation of lithium ions within brownmillerite structure, as reported in literature.[10] At 0.5 V, after 9 h discharge, the entire diffraction signals intensity continues to decrease and since 0.3 V (at the end of the long plateau). Unfortunately, it was not possible to clearly identify any phases being all materials neither constituted by CFO or Li_2O or CaO. Such observation agrees with the reported in literature and one can speculate about the possible formation of an amorphous or extremely poorly crystalline particles.[37,39,40] However, as observable from the diffraction pattern acquired at the end of the charge, initial phase peaks are recovered with smaller intensities thus suggesting calcium ferrite partial re-crystallization.

Impact of Doping on Performance in Lithium Cell (Mn, Ni, Cu)

Doped materials have been tested in lithium cells under same experimental conditions described in previous Section for the pristine undoped CFO. The first galvanostatic cycle is shown in the Figure 5a for all doped materials. In the first cycle, the doped materials show a potential profile with comparable shape in respect to the undoped material: all the materials show similar plateau at ca. 1.5 V and under 0.5 V, respectively.

Research Article
doi.org/10.1002/batt.202400063
Chemistry Europe
European Chemical Societies Publishing

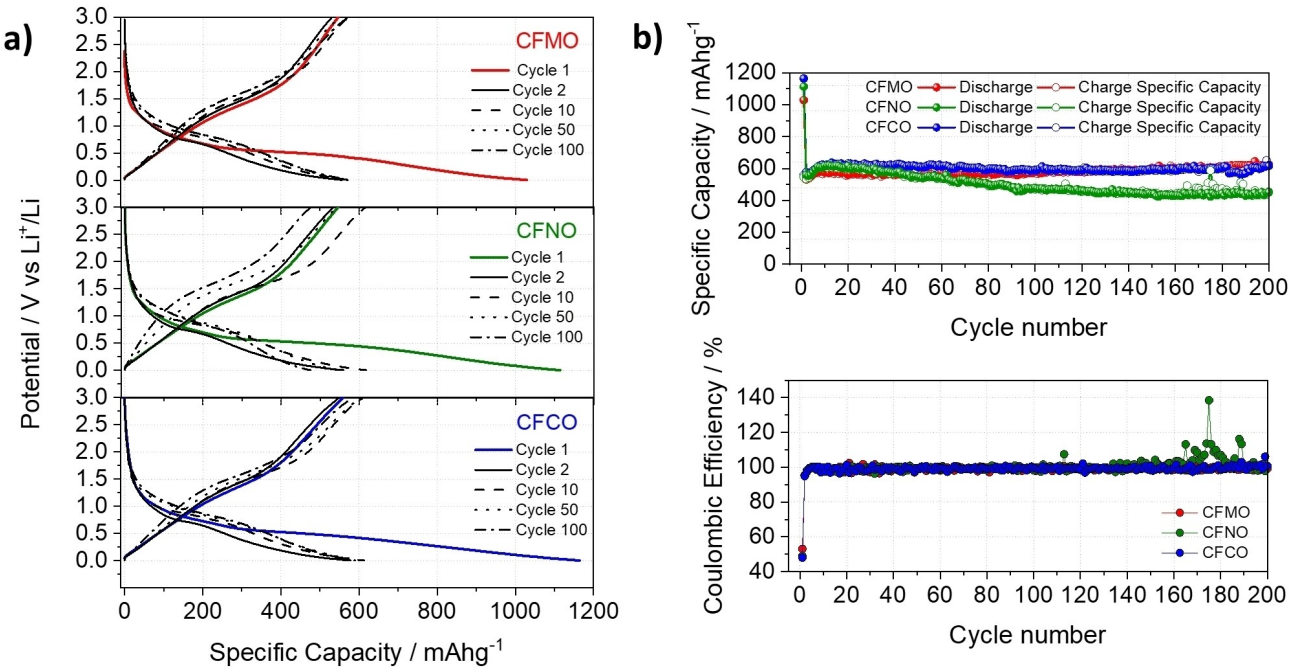

Figure 5. a) potential profiles and b) cycling performance of CFMO, CFNO and CFCO electrodes in lithium cells by galvanostatic cycling at C/10.

First discharge and charge specific capacities are listed in Table 3 for all the different types of calcium ferrites. Apparently, the nature of the doping does not determine a systematic increase of specific discharge capacity, not even in the case of Cu doping, despite the much higher conductivity of this sample. However, in the case of Mn and Cu doped samples, we can observe an increase of cycling stability (see Figure 5b). In fact, after 100 cycles, capacity retention, evaluated from 10th to 100th cycles, is 81 % for CFO, 76.6 % for CFNO, 96.2 % for CFCO, and 98.8 % for CFMO.

The negligible effect of the higher conductivity of the CFCO sample must be related to the large amount of super P carbon always added to the electrode formulation, which levels the performances of all the samples. As a confirmation, AC impedance spectra were collected on several cells and impedance evolution was followed upon cycling. Figure S6 reports the Nyquist plot obtained at the end of the first cycle at C/10. From the fitting of the plots, the charge transfer resistance was calculated from the deconvolution of the two semicircles in the high frequency region, as: 49 ± 10 Ω for CFO, 62 ± 10 Ω for CFMO, 69 ± 10 Ω for CFNO and 53 ± 10 Ω for CFCO. The results are always similar, with a small variability that is only poorly related to the sample identity, also considering replica results.

To further test the electrochemical performance of our samples, additional galvanostatic cycling while varying the current densities from ~60 mA g^{-1} (C/10) to ~1200 mA g^{-1} (2 C) have been recorded in the potential cutoff range 0.005-3 V vs Li$^+$/Li. Apart the C-rate check for 10 cycles, the testing protocol also involved additional 50 cycles at ~60 mA g^{-1} (C/10) (see the capacity evolution shown in Figure 6b). Discharge specific capacities for CFO are ca. 620, 560, 450, 280, 130 mAh g^{-1} for C/10, C/5, C/2, 1 C and 2 C, respectively (Figure 6a). At all the current densities coulombic efficiency is particularly large well above 99 %, as shown in Figures 6a and 6b. Overall doped materials have performance comparable to CFO at low current densities (C/10, C/5). However, at high C-rates some differences can be noted. At 1 C (~600 mA g^{-1}) CFNO performed better than CFO, with a 45 mAh g^{-1} specific capacity increase (from 280 to 325). Instead, CFMO performed similarly to CFO, with only a 20 mAh g^{-1} (from 280 to 260), whilst CFCO showed a

Table 3. Comparison of specific capacity, Coulombic efficiency and capacity retention values obtained for all the samples.

Sample name	Disch. Spec. Cap. (mAh g^{-1}) 1st cycle	Charge Spec. Cap. (mAh g^{-1}) 1st cycle	Coulombic Efficiency (%) 1st cycle	Charge Spec. Cap. (mAh g^{-1}) 10th cycle	Charge Spec. Cap. (mAh g^{-1}) 100th cycle	Capacity Retention[a] (%)
CFO	1227	594	48	644.6	529	81
CFMO	1029	546	53	574	567	98.8
CFNO	1114	546	49	615	471	76.6
CFCO	1164	560	48	611	588	96.2

[a] Capacity retention was calculated from 10th to 100th cycle.

Research Article
doi.org/10.1002/batt.202400063
Chemistry Europe
European Chemical Societies Publishing

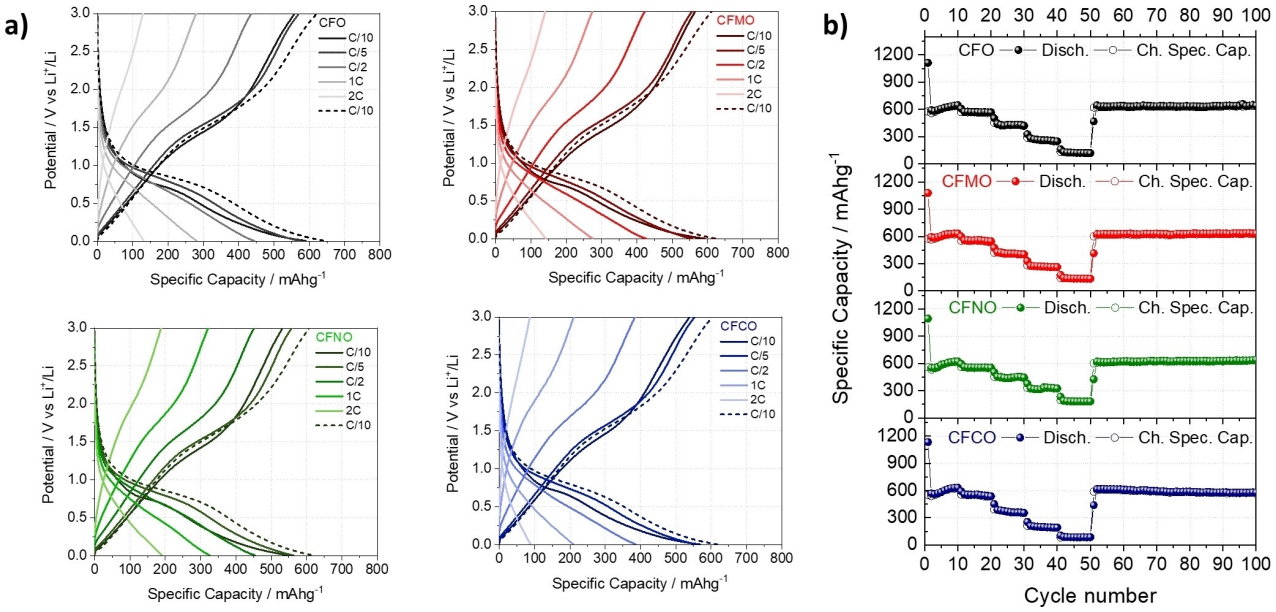

Figure 6. Rate Capability Test of undoped and doped CFOs samples in lithium half-cell by galvanostatic cycling.

70 mAh g^{-1} decrease (from 280 to 210) compared to the same material. At 2 C (~1200 mA g^{-1}), this trend was partially repeated, as CFNO performed the best among the doped materials and surpassing the properties of CFO, whilst CFMO performed similarly, and CFCO performed the worst with ca. 90 mAh g^{-1} of specific discharge capacity.

Conclusions

With the present work, we demonstrated the synthesis of calcium ferrites through a solid-state route with HEBM activation. The procedure is highly scalable and proved to be efficient for the effective doping of the initial material with Mn, Ni, and Cu.

Diffraction measurements demonstrated modifications in cell parameters of doped samples and gave proof of deformations in their crystalline order. On the other hand, Raman Spectroscopy could suggest changes in the short distance order of doped materials. Furthermore, uniform distribution of the dopants was observed on the particles surfaces of doped materials through EDX-SEM. More work should be needed to understand how the dopants are located within the material structure, and the reasons behind the structural modification. As observed with SEM, the samples showed large differences in terms of morphology. This is the case of CFNO and CFCO samples, where the introduction of the dopant within CFO structure determined a change in the morphology, eventually drastic. Therefore, we explored the electrochemistry of calcium ferrites in lithium-ion batteries, and the possible changes given by the doping. The processed CFO composite anode delivered stably ca. 600 mAh g^{-1} at 60 mA g^{-1} and ca. 130 mAh g^{-1} at 1200 mA g^{-1}. When doped, specific capacity slightly decreases in value. While, except for CFNO, capacity retention overcome the 90%, approaching to 99% in the case of CFMO, observing the following scale: CFMO > CFCO > CFO > CFNO.

Regarding the behavior at high cycling rates, the trend changed and had the following order: CFNO > CFMO~CFO > CFCO.

In conclusion, this work offers an investigation on the structural complexities of brownmillerite-type doped calcium ferrites. This material class demonstrated promising results as a high-capacity and fast-charging anode material for lithium-ion batteries, satisfying also the markets needs in terms of scalability of the synthesis and abundance of raw materials.

Experimental Section

Materials and Methods

Iron oxide (Fe_2O_3), calcium carbonate ($CaCO_3$), manganese oxide (Mn_2O_3), nickel oxide (NiO), copper oxide (CuO) were used as starting reagents. All the chemicals were purchased from Sigma Aldrich and used as received.

$Ca_2Fe_{2-x}M_xO_5$ (M = Mn, Ni, or Cu, x = 0, 0.1) samples were prepared following a two-step synthesis procedure, consisting of a High Energy Ball Milling (HEBM) and a calcination steps. The reactants were weighted in stoichiometric proportions and milled for 10 h in a planetary-type mill (Retsch PM 100, Germany) with 80 mL agate stone jar and a ball-to-powder ratio (BPR) of ca. 1/15 and an occupied volume percentage (V_{occ}) of ca. 17%. HEBM was conducted at 500 rounds-per-minute (rpm) for 10 hours alternating 1 hour of milling to 30 minutes of rest.

Once collected, the milled powder (still consisting of a mixture of $CaCO_3$ and Fe_2O_3, see Figure S7) has been subjected to a thermal treatment according to the refs. [21] and [26].

The powder was pressed into pellet with diameter of 25 mm, under 5 ton and calcinated in a muffle furnace (Carbolite CWF 1200, UK)

at 1000 °C for 10 h, with temperature-ramping-rate of 3 °C/min. The pellet was then grinded into mortar and resulting powders were stored in a vial for further characterization.

Electrical conductivity of the as prepared samples was measured on the pellets recovered at the end of thermal treatment, by the use of 4-point probe method. The measurements were performed at 20 °C by Mitsubishi Resistivity Meter Loresta GX (MCP–T1700) using a linear probe with electrodes distance of 5 mm.

Elemental analysis was performed with Atomic Absorption Spectroscopy (ContrAA300 – Analytik Jena AG).

Powder phase analysis was performed with an X-ray diffractometer (XRD, Rigaku SmartLab, Japan) with Bragg-Brentano geometry and CuKα radiation. Crystallographic informations were obtained through Rietveld Refinement with GSAS-II.[41] The refinement phase was derived from PDF Card: 00–047-1744. For doped samples, phases were modified during the refinement, substituting 5% of Fe^{3+} ions with proper dopants.

Raman spectra were acquired with a DILOR LabRam confocal micro-Raman with a He–Ne laser source at 632.7 nm and a CCD cooled detector. Si was used as calibrating standard for the energy scale.

The morphology of the synthesized powder was observed by means of the scanning electron microscopic (SEM) analysis with a Field-Emission-Gun (FEG)-SEM microscope (ZEISS Gemini LEO 1530, Germany) with acceleration voltages of 10 kV and 20 kV and a resolution of 100, 200 nm, 1 μm.

X-ray photoelectron spectroscopy (XPS) measurements were conducted utilizing a conventional non-monochromatized X-ray source (Al Kα = 1487 eV) and a hemispherical electron energy analyzer. These measurements were carried out within a dedicated chamber of the NFFA UHV MBE-cluster system.[42] To fix the powders onto the sample holder, conductive carbon tape was employed. The samples were positioned at a 45° angle relative to the incident beam, allowing for the investigation of an approximately 1 mm^2 area at a depth of around 1 nm. Acquisition of the Fe 2p, 2p Ca, and valence band spectra was accomplished using a pass energy of 100 eV and a dwell time of 1000 ms. The survey parameters mirrored those of the core level spectra, with the only exception being a dwell time of 500 ms. CasaXPS software was employed for the fitting of core levels.[43] The energy alignment was done using the 4fAu core level of the sputtered gold foil located inside the XPS chamber.

Electrode Preparation and Electrochemical Characterization

HEBM was used also to prepare electrodes for electrochemical characterization. Specifically, calcium ferrite powders were milled together with a conductive carbon SuperP in a mass ratio of 5:3. The purpose was to improve electron conductivity in the electrodes.

In this case, HEBM was conducted for 5 h at 25 Hz with BPR ~ 1/15 and V_{occ} ~ 17% with a Vibratory Mill (Retsch MM400, Germany) using stainless steel 50 ml jar and 12 mm balls. The powder mixture was then mixed with polyvinylidene difluoride (PVDF) binder in mass ratio of 4:1 into a mortar (calcium ferrite: SuperP: PVDF mass ratio percentage = 50:30:20). Thus, the mixed powders were dispersed into N-methyl-2-pyrrolidone (NMP) to get a homogeneous slurry which was coated onto a copper foil by doctor blade, with 200 μm thickness. The electrodes preparation was conducted in a Dry Room at 20 °C and with a Dew Point of −70 °C.

The foil was dried at 50 °C for 3 h in a vacuum oven to remove NMP from the slurry. Then, the electrodes were cut into discs of 10 mm diameter, and they were dried at 110 °C overnight in a Büchi oven under vacuum (BÜCHI Labortechnik).

The electrodes were tested in different types of cell setups. For galvanostatic cycling and Rate Capability tests, we used coin cells (CR2032), whilst we used Swagelok-like two electrode cells for ex-situ tests. All cells were assembled with as-prepared electrode, lithium metal foil, and Whatman GF/A separator as the working electrode, counter electrode, and separator, respectively. LP30, 1 M $LiPF_6$ in ethylene carbonate (EC) and dimethyl carbonate (DMC) 1:1 v/v, was used as electrolyte.

Electrochemical cells were assembled in an Ar-filled glovebox (Jacomex GP(Concept)) with O_2 and H_2O levels below 1 ppm.

The galvanostatic charge-discharge cycling performance was investigated at room temperature with a multichannel galvanostat (Maccor S4000). The cells were galvanostatically discharged/charged from 0.005 to 3 V vs Li/Li^+, with C/10 rate (1 C = 591 mAh g^{-1}). We also performed Rate Capability (RC) tests with the following sequence of C-rates: C/10, C/5, C/2, 1 C and 2 C.

Potentiostatic Electrochemical impedance Spectroscopy (PEIS) were performed at room temperature on a multichannel potentiostat (Biologic VMP-3e), using an alternate voltage with an amplitude of 10 mV from a frequency of 100 kHz to a frequency of 0.1 Hz. The impedance spectra were fitted with Z-fit tool implemented in the software of Biologic EC-lab.

All the electrochemical tests were conducted in a climatic chamber at 20 °C and every measurement has been repeated assembling 3 cells at least.

Ex-Situ XRD Experiment

To perform ex-situ diffraction experiment, calcium ferrite-based electrodes have been assembled in lithium cells and cycled at different state of discharge/recharge in galvanostatic mode at C/20 by the use of Maccor system. At the end of the procedure, the cells were opened in dry room (20 °C, Dew Point −70 °C), the electrodes recovered, washed in DMC several times and dried.

To avoid support interference, calcium ferrite-based electrodes were prepared without the copper support. These self-standing electrodes were prepared mixing the active material with SuperP and PVdF in mass proportions of 8:1:1, similarly to the procedure described above.

Supporting Information

The authors have cited additional references within the Supporting Information.

Deposition Numbers 2350463 for CFO, 2350464 for CFMO, 2350465 for CFNO and 2350466 for CFCO contain the supplementary crystallographic data for this paper. These data are provided free of charge by the joint Cambridge Crystallographic Data Centre and Fachinformationszentrum Karlsruhe http://www.ccdc.cam.ac.uk/structures.

Acknowledgements

We would like to thank Dr. Pier Giorgio Schiavi of Sapienza University for A.A.S measurements. G.S., P.R., S.B. and L.S. acknowledge Lazio Innova for the funding in the frame of the ACTEA project, FESR Fondo Europeo di Sviluppo Regionale 2014–2020, POR code A0375E0019. L.S. and F.B. acknowledge IPCEI project European Battery Innovation (EuBatIn) funded by Ministero dell'ambiente e della sicurezza energetica. A.C and S.B would like to thank the NEST – Network for sustainable energy transition Foundation and received funding from the European Union Next-GenerationEU (PIANO NAZIONALE DI RIPRESA E RESILIENZA (PNRR) – MISSIONE 4 COMPONENTE 2, INVESTIMENTO 1.3, PE0000021). This manuscript reflects only the authors' views and opinions, neither the European Union nor the European Commission can be considered responsible for them.

Conflict of Interests

The authors declare no conflict of interest.

Data Availability Statement

The data that support the findings of this study are available from the corresponding author upon reasonable request.

Keywords: energy conversion · Li-ion batteries · Solid-phase synthesis · ternary iron oxides

[1] IEA, Grid-Scale Storage, Paris, **2022**.
[2] IEA, Electric Vehicles, Paris, **2022**.
[3] L. Mauler, X. Lou, F. Duffner, J. Lekera, *Energy Advances* **2022**, *1*, 136–145.
[4] I. Y. L. Hsieh, M. S. Pan, Y. M. Chiang, W. H. Green, *Appl Energy* **2019**, *239*, 218–224.
[5] IEA, The Role of Critical Minerals in Clean Energy Transitions, Paris, **2021**.
[6] "Graphite: Supply chain challenges & recommendations for a critical mineral - HCSS," can be found under https://hcss.nl/report/graphite-supply-chain-challenges-recommendations-for-a-critical-mineral/, n.d.
[7] S. Wei, D. Di Lecce, R. M. D. Agostini, J. Hassoun, *ACS Appl Energy Mater* **2021**, 8340–8349.
[8] S.-H. Yu, S. H. Lee, D. J. Lee, Y.-E. Sung, T. Hyeon, *Small* **2016**, *12*, 2146–2172.
[9] N. Sharma, K. M. Shaju, G. V. Subba Rao, B. V. R. Chowdari, *Electrochim Acta* **2004**, *49*, 1035–1043.
[10] S. K. Sundriyal, Y. Sharma, *ACS Appl Energy Mater* **2020**, *3*, 6360–6373.
[11] S. K. Sundriyal, Y. Sharma, *Appl Surf Sci* **2021**, *560*, 150055.
[12] P. Zhu, G. Yang, X. Sun, Q. Cao, Y. Zhao, R. Ding, E. Liu, P. Gao, *New Journal of Chemistry* **2023**, *47*, 11102–11109.
[13] K. Zhang, S. Liang, X. Yin, P. Gao, R. Ding, E. Liu, *J Solid State Chem* **2020**, *286*, 121300.
[14] V. Cascos, R. Martínez-Coronado, J. A. Alonso, M. T. Fernández-Díaz, *Int J Hydrogen Energy* **2015**, *40*, 5456–5468.
[15] K. Gupta, S. Singh, M. S. Ramachandra Rao, *Nano Energy* **2015**, *11*, 146–153.
[16] D. S. Vavilapalli, S. Banik, R. G. Peri, B. Muthuraaman, M. Miryala, M. Murakami, K. Alicja, K. Asokan, M. S. Ramachandra Rao, S. Singh, *Sci Rep* **2020**, *10*, 1–13.
[17] S. Thundiyil, C. P. Vinod, S. Kurungot, R. N. Devi, P *hysical Chemistry Chemical Physics* **2020**, *22*, 15520–15527.
[18] K. Gupta, S. Singh, M. Ceretti, M. S. R. Rao, W. Paulus, *Physica Status Solidi (A) Applications and Materials Science* **2013**, *210*, 1771–1777.
[19] S. Dhankhar, K. Gupta, G. Bhalerao, N. Shukla, M. Chandran, B. Francis, B. Tiwari, K. Baskar, S. Singh, *RSC Adv* **2015**, *5*, 92549–92553.
[20] E. C. Okpara, O. B. Wojuola, O. E. Fayemi, O. A. Oyewo, D. C. Onwudiwe, *J Inorg Organomet Polym Mater* **2022**, *32*, 3445–3458.
[21] L. A. Isupova, S. V. Tsybulya, G. N. Kryukova, A. A. Budneva, E. A. Paukshtis, G. S. Litvak, V. P. Ivanov, V. N. Kolomiichuk, Y. T. Pavlyukhin, V. A. Sadykov, *Kinetics and Catalysis* **2002**, *43*, 122–129.
[22] E. Asenath-Smith, S. T. Misture, D. D. Edwards, *J Solid State Chem* **2011**, *184*, 2167–2177.
[23] M. Ceretti, A. Piovano, A. Cousson, T. Berthier, M. Meven, G. Agostini, J. Schefer, O. Hernandez, C. Lamberti, W. Paulus, *CrystEngComm* **2012**, *14*, 5771–5776.
[24] S. Dhankhar, G. Bhalerao, S. Ganesamoorthy, K. Baskar, S. Singh, *J Cryst Growth* **2017**, *468*, 311–315.
[25] E. Asenath-Smith, I. N. Lokuhewa, S. T. Misture, D. D. Edwards, *J Solid State Chem* **2010**, *183*, 1670–1677.
[26] B. F. Amorim, M. A. Morales, F. Bohn, A. S. Carriço, S. N. De Medeiros, A. L. Dantas, *Physica B Condens Matter* **2016**, *488*, 43–48.
[27] I. Antunes, L. C. M. Ruivo, L. A. C. Tarelho, A. A. Yaremchenko, J. R. Frade, *Ceram Int* **2022**, *48*, 34025–34032.
[28] S. Thundiyil, C. P. Vinod, S. Kurungot, R. N. Devi, *Physical Chemistry Chemical Physics* **2020**, *22*, 15520–15527.
[29] B. H. Toby, R. B. Von Dreele, *Journal of Applied Crystallography* **2013**, *46*, 544–549.
[30] A. Piovano, M. Ceretti, M. R. Johnson, G. Agostini, W. Paulus, C. Lamberti, *Journal of Physics Condensed Matter* **2015**, *27*, 225403.
[31] K. Gupta, S. Singh, M. S. Ramachandra Rao, *Nano Energy* **2015**, *11*, 146–153.
[32] T. L. Phan, N. Tran, D. H. Kim, P. T. Tho, B. T. Huy, T. N. Dang, D. S. Yang, B. Lee, *Journal of the American Ceramic Society* **2018**, *101*, 2181–2189.
[33] Q. E. Stahl, G. J. Redhammer, G. Tippelt, A. Reyer, *Phys Chem Miner* **2019**, *46*, 271–298.
[34] T. Xu, X. Wang, H. Zhao, B. Xiao, D. Liu, W. Liu, *Appl Catal B* **2023**, *320*, 122010.
[35] D. Wilson, M. A. Langell, *Appl Surf Sci* **2014**, *303*, 6–13.
[36] D. S. Vavilapalli, K. Srikanti, R. Mannam, B. Tiwari, M. Mohan Kant, M. S. R. Rao, S. Singh, *ACS Omega* **2018**, *3*, 16643–16650.
[37] S. Permien, S. Indris, M. Scheuermann, U. Schürmann, V. Mereacre, A. K. Powell, L. Kienle, W. Bensch, *J Mater Chem A Mater* **2015**, *3*, 1549–1561.
[38] S. K. Sundriyal, Y. Sharma, *J Electrochem Soc* **2020**, *167*.
[39] S. Permien, S. Indris, U. Schürmann, L. Kienle, S. Zander, S. Doyle, W. Bensch, *Chemistry of Materials* **2016**, *28*, 434–444.
[40] Y. Wang, D. Su, A. Ung, J. H. Ahn, G. Wang, *Nanotechnology* **2012**, *23*, 4–10.
[41] B. H. Toby, R. B. Von Dreele, *J Appl Crystallogr* **2013**, *46*, 544–549.
[42] G. Vinai, F. Motti, A. Y. Petrov, V. Polewczyk, V. Bonanni, R. Edla, B. Gobaut, J. Fujii, F. Suran, D. Benedetti, F. Salvador, A. Fondacaro, G. Rossi, G. Panaccione, B. A. Davidson, P. Torelli, *Review of Scientific Instruments* **2020**, *91*, DOI 10.1063/5.0005302/991082.
[43] N. Fairley, V. Fernandez, M. Richard-Plouet, C. Guillot-Deudon, J. Walton, E. Smith, D. Flahaut, M. Greiner, M. Biesinger, S. Tougaard, D. Morgan, J. Baltrusaitis, *Applied Surface Science Advances* **2021**, *5*, 100112.

Manuscript received: January 29, 2024
Revised manuscript received: April 23, 2024
Accepted manuscript online: May 18, 2024
Version of record online: June 27, 2024